



Article

Intricacies of Opening Geometry Detection in Terrestrial Laser Scanning: An Analysis Using Point Cloud Data from BLK360

Jinman Jung ¹, Taesik Kim ², Hong Min ³, Seongmin Kim ⁴ and Young-Hoon Jung ^{4,*}¹ Department of Computer Engineering, Inha University, Incheon 22212, Republic of Korea; jmjung@inha.ac.kr² Department of Civil and Environmental Engineering, Hongik University, Seoul 04066, Republic of Korea; taesik.kim@hongik.ac.kr³ School of Computing, Gachon University, Seongnam 13120, Republic of Korea; hmin@gachon.ac.kr⁴ Department of Civil Engineering, Kyung Hee University, Yongin-si 17104, Republic of Korea; tksm@khu.ac.kr

* Correspondence: jyounghoon@khu.ac.kr

Abstract: This study investigates the use of terrestrial laser scanning (TLS) in urban excavation sites, focusing on enhancing ground deformation detection by precisely identifying opening geometries, such as gaps between pavement blocks. The accuracy of TLS data, affected by equipment specifications, environmental conditions, and scanning geometry, is closely examined, especially with regard to the detection of openings between blocks. The experimental setup, employing the BLK360 scanner, aimed to mimic real-world paving situations with varied opening widths, allowing an in-depth analysis of how factors related to scan geometry, such as incidence angles and opening orientations, influence detection capabilities. Our examination of various factors and detection levels reveals the importance of the opening width and orientation in identifying block openings. We discovered the crucial role of the opening width, where larger openings facilitate detection in 2D cross-sections. The overall density of the point cloud was more significant than localized variations. Among geometric factors, the orientation of the local object geometry was more impactful than the incidence angle. Increasing the number of laser beam points within an opening did not necessarily improve detection, but beams crossing the secondary edge were vital. Our findings highlight that larger openings and greater overall point cloud densities markedly improve detection levels, whereas the orientation of local geometry is more critical than the incidence angle. The study also discusses the limitations of using a single BLK360 scanner and the subtle effects of scanning geometry on data accuracy, providing a thorough understanding of the factors that influence TLS data accuracy and reliability in monitoring urban excavations.

Keywords: terrestrial laser scanning; opening geometry; point cloud data; laser incidence angle; scanning geometry



Citation: Jung, J.; Kim, T.; Min, H.; Kim, S.; Jung, Y.-H. Intricacies of Opening Geometry Detection in Terrestrial Laser Scanning: An Analysis Using Point Cloud Data from BLK360. *Remote Sens.* **2024**, *16*, 759. <https://doi.org/10.3390/rs16050759>

Academic Editors: Bahareh Kalantar, Alfian Abdul Halin and Husam A. H. Al-Najjar

Received: 26 November 2023

Revised: 15 February 2024

Accepted: 19 February 2024

Published: 21 February 2024



Copyright: © 2024 by the authors. Licensee MDPI, Basel, Switzerland. This article is an open access article distributed under the terms and conditions of the Creative Commons Attribution (CC BY) license (<https://creativecommons.org/licenses/by/4.0/>).

1. Introduction

In urban areas, such as residential or commercial zones, excavations pose significant challenges due to the potential impacts on neighboring structures, utilities, and pedestrians. Traditional surveying methods have often been insufficient in comprehensively determining the impacts of such excavations. For instance, while asphalt and concrete pavements adjacent to the excavations might not visibly settle, the underlying soil can be affected and deformed. More flexible pedestrian block pavements, however, can manifest noticeable deformations, resulting in changes in the gaps between blocks. Conventional ground movement detection methods, such as affixing steel nails for level surveys, sometimes miss significant shifts. Hence, monitoring the variations in the gaps between pavement blocks, illustrated in Figure 1, offers a more comprehensive perspective on ground deformation due to urban excavation.



Figure 1. (a) Supporting wall and safety fence standing at an excavation site; (b) block pavement for pedestrians adjacent to the safety fence outside the excavation site; (c) example of misaligned blocks adjacent to the safety fence; (d) example of severe distortion in the block pavement.

Terrestrial laser scanning (TLS) has emerged as a modern approach to obtaining intricate surface data. This aids in constructing accurate digital models and permits extensive data collection during excavation processes [1]. Despite its potential, the accuracy of TLS can differ based on the monitored objects and equipment specifications. For example, our study employs the Leica BLK360 scanner from Leica Geosystems (Heerbrugg, Switzerland) [2]. According to the manufacturer, this scanner offers an accuracy of 6 mm at a distance of 10 m and 8 mm at 20 m. Although the single-point accuracy of TLS might fall short of traditional methods, such as level and total station surveys [3,4], the accuracy can be enhanced through the intricate object extraction process [5,6]. Unfortunately, TLS does not inherently capture specific features like the gaps or openings between blocks, which represent our study's focus. These features become discernible post the modeling of the extracted scanned point clouds [7].

Geometrically, opening geometries between pavement blocks can be categorized as specific forms of cracks in flat surfaces. Many studies have focused on devising computational techniques for detecting cracks in surfaces like concrete, asphalt, and timber [8–17]. Compared to photogrammetry, using TLS for crack detection is superior, especially for assessing crack depths. Laefer et al. [18] present the fundamental mathematics and experimental validation for determining the minimum detectable crack width in unit-based masonry using TLS. However, guaranteeing the integrity of data remains a challenge, especially when detecting intricately structured cracks [19,20].

The quality and precision of point cloud data are influenced by several factors, such as instrumental mechanisms, environmental conditions, object surface properties, scan geometry, and object geometry [21–23]. Boehler et al. [7] present a comprehensive study on the accuracy of 3D laser scanners, comparing various models through standardized tests to assess the quality of the data that they produce. The effects of the scan geometry, focusing on the laser incidence angle and the range of the beam, have been intensively investigated [24–28]. The effects of the scan geometry have been extensively investigated in various fields, such as tunnel inspection [29], structural deflection [30], soil surface roughness assessment [31], rock surface roughness [32], and forests [33]. Gerbino et al. [34] examined how the scanner-to-object orientation, ambient lighting, and scanner settings affect the accuracy of 3D laser scanning in manufacturing inspection processes. Notably, previous studies typically worked within certain environments, such as surveying only flat or curved surfaces. However, many geometric aspects of scanning objects with localized openings have yet to be thoroughly investigated.

In this study, we investigate the impact of multiple factors related to scan geometry on the detection of openings between blocks. Specifically, we examine the incidence angles, opening dimensions, the orientations of localized opening geometries, the numbers of laser points beaming into the opening, and point cloud densities. Through nine unique metrics, we identify correlations between these parameters and their detection level. Our results offer a ranked list of these factors, offering crucial insights for improved measurement approaches in ground movement detection scenarios in the urban excavation.

2. Materials and Methods

2.1. Scanner

The BLK360 TLS [2] was used to collect point clouds of the test specimens. Table 1 lists the technical specifications of TLS. BLK360 operates based on the scanning optics of a vertically rotating mirror on a horizontally rotating base. A rotating optical mirror is used to transmit the laser beam to an object and receive a return beam. The point accuracy is expressed in Cartesian coordinates and is different from the measurement range. The scan angle step indicates the ability to resolve two equally intense point sources on adjacent lines of sight. The field of view (FOV) offers possible angle-scanning ranges in the horizontal and vertical directions. In the standard setup for upward scanning, the vertical FOV is limited to 300°, which results in the ground view beneath the scanner being missed. The scanner had a full view of the ground beneath the scanner upon the flipping of the Leica BLK360 scanner downward to the ground.

Table 1. Technical specification of TLS [2].

Description	Value
System	Leica BLK360
Metrology method	Pulse-based (time of flight)
Laser pulse duration	4×10^{-9} s
Pulse repetition frequency (PRF)	1,440,000 Hz
Beam divergence (FWHM, full range)	0.0004 rad
Beam diameter	2.25 mm at the front window
Mirror rotation frequency	30 Hz
Base rotation frequency	0.0025 Hz
Min./max. range (m)	0.6 m/60 m
Range accuracy	4 mm at 10 m and 7 mm at 20 m
Point accuracy (1 sigma)	6 mm at 10 m and 8 mm at 20 m
Scan angle step size, Δ (°) *	0.00751
Scan angle accuracy (°)	0.0111
Field of view H/V (°)	360/300

* The scan angle step size was estimated based on the angular velocity of the mirror, base rotation, and pulse repetition frequency.

2.2. Test Specimens

In lieu of concrete pavement blocks, which often exhibit dimensional inconsistencies during mass production, we employed black-coated metal plates to meticulously construct test specimens. Each plate has the dimension of 25 mm in width, 25 mm in thickness, and 145 mm in length. These specimens emulate four aligned paving blocks with a specified opening geometry. Figure 2 describes these specimens with varying opening widths, achieved by positioning pairs of metal blocks. Figure 2a illustrates the configuration of the scanner and the opening geometry specimen.

As depicted in Figure 2a, the top view reveals the opening geometry as a rectangle, characterized by a longer “primary edge” of length b and a shorter “secondary edge” of length w . The reference point is set as the midpoint of the primary edge, shown in Figure 2a, and the reference line is the horizontal line between the reference point and the ground-projected center of the scanner. We established the opening width, w , between the two blocks by 2, 5, 10, 15, and 20 mm, as shown in Figure 2c–g. To maintain the desired

width, detachable white plastic spacers, calibrated to an accuracy of 0.01 mm, were inserted between the blocks, as can be seen in Figure 2.

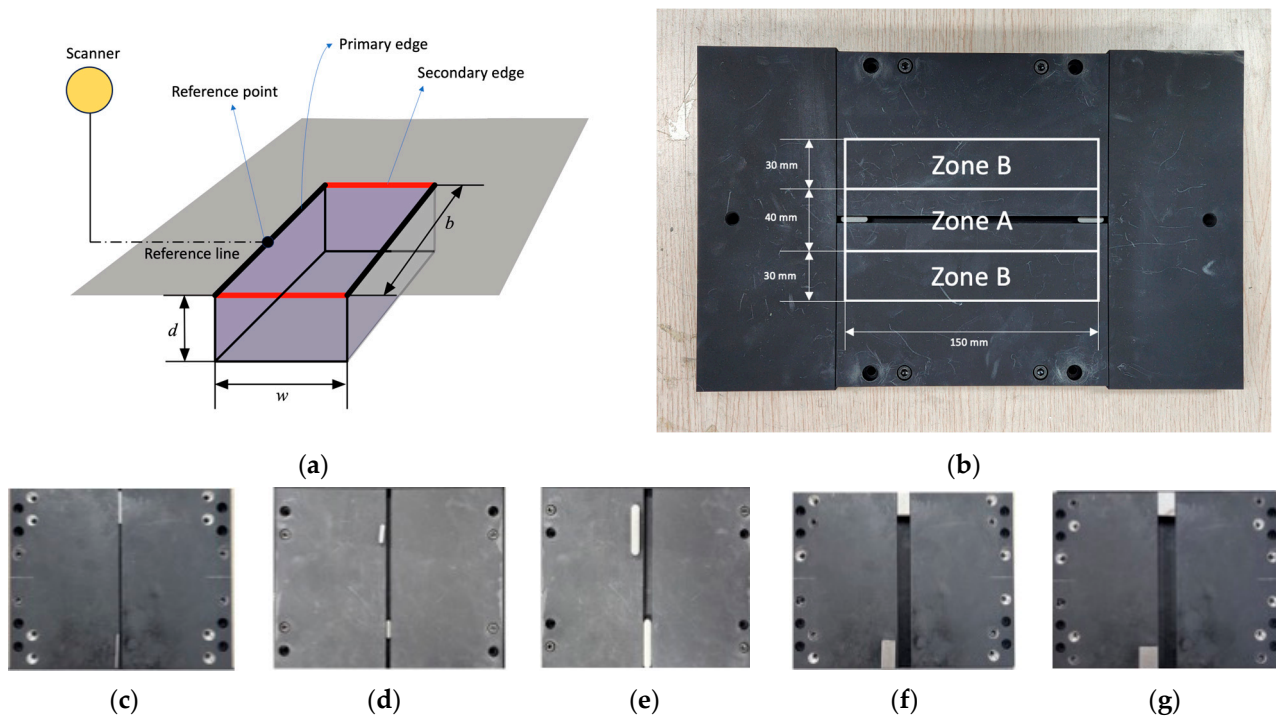


Figure 2. (a) Test specimens with the opening width of (c) 2 mm, (d) 5 mm, (e) 10 mm, (f) 15 mm, and (g) 20 mm. (b) The point densities of Zones A and B were evaluated separately.

Liu et al. [35] emphasize that the density of point clouds in single-scan TLS is closely linked to object geometry, which, when combined with scan geometry and instrumental parameters, quantitatively influences the distribution of points. Consequently, it is necessary for the point cloud data from the scanned specimen to be segregated into two distinct zones: ‘Zone A’, which encompasses the complex geometry of the opening, and ‘Zone B’, which comprises the adjoining flat surface. Figure 2b delineates the dimensions of Zones A and B, which, respectively, cover areas of 6000 mm² and 9000 mm². After scanning, the point densities of Zones A and B are designated by ρ_A and ρ_B , respectively.

2.3. Test Configurations

Figure 3 illustrates the configuration of the scanner and the test specimen. The incidence angle θ is defined as the angle between the laser beam vector and the normal vector of a surface of the test specimen at the reference point. The angle α describes the orientation of the opening geometry relative to the scanner, specifically, the angle between the normal vector of the primary edge and the reference line in the horizontal plane. Figure 3 also shows how the test specimen was configured prior to scanning at incidence angles θ of 0°, 10°, 20°, 30°, 45°, or 60°, and the orientation of the opening geometry, $\alpha = 0^\circ, 45^\circ, \text{ and } 90^\circ$.

Figure 4 describes the various symbols used for the geometric condition of the test configuration. The vertical gap from the scanner to the specimen’s level surface is denoted as H , which is constantly 107 cm in all the test configurations. The distance L represents the span between the ground-projected center of the scanner and the reference point. β denotes the angle offset of the current laser beam from the reference line in the horizontal plane, with L_β being the line from the scanner to the laser point of contact with the edge. Figure 4a focuses on the cross-section of the opening geometry as it interacts with the laser beam where θ_β is the incidence angle of the laser at an arbitrary β , with θ being the angle when $\beta = 0$. The depth of the opening in the cross-sectional view is d . The width, w_β , deviates

from w depending on β . Figure 4a illustrates that the laser beam does not reach the base of the opening completely, with n_w being the number of the laser beam points reaching the base. The critical angle at which the laser interacts with the opening's base corner is $\theta_{\beta 0}$. For θ_β less than $\theta_{\beta 0}$, the laser touches the base of the opening. Otherwise, it only interacts with its vertical face, with n_d being the number of the laser beam points reaching the face. Table 2 summarizes the geometric conditions of the test configurations.

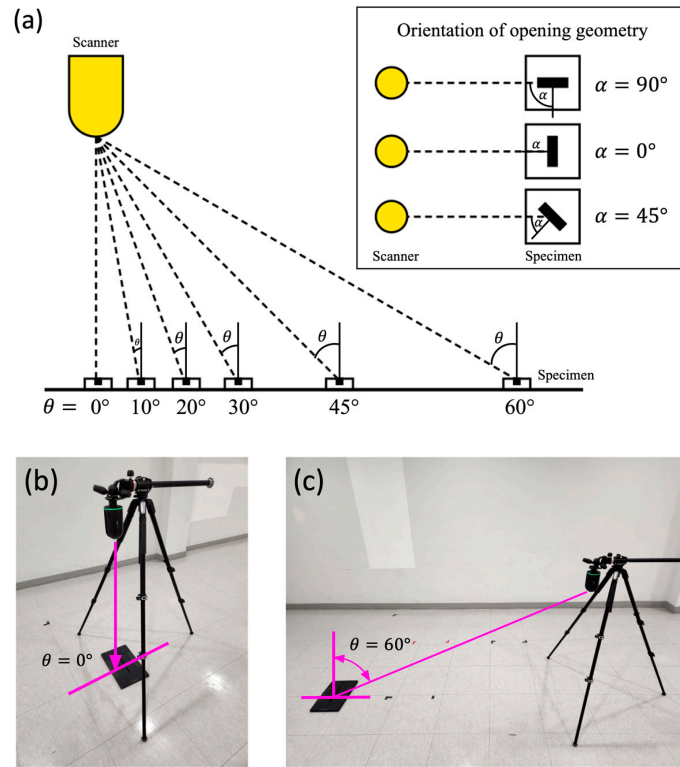


Figure 3. Configuration of the specimen and the scanner at (a) the incidence angle, θ , and the orientation of the opening geometry, α . The scanner and the specimens were configured at the incidence angles of (b) 0° and (c) 60° . The TLS was flipped downward to scan the specimen on the ground.

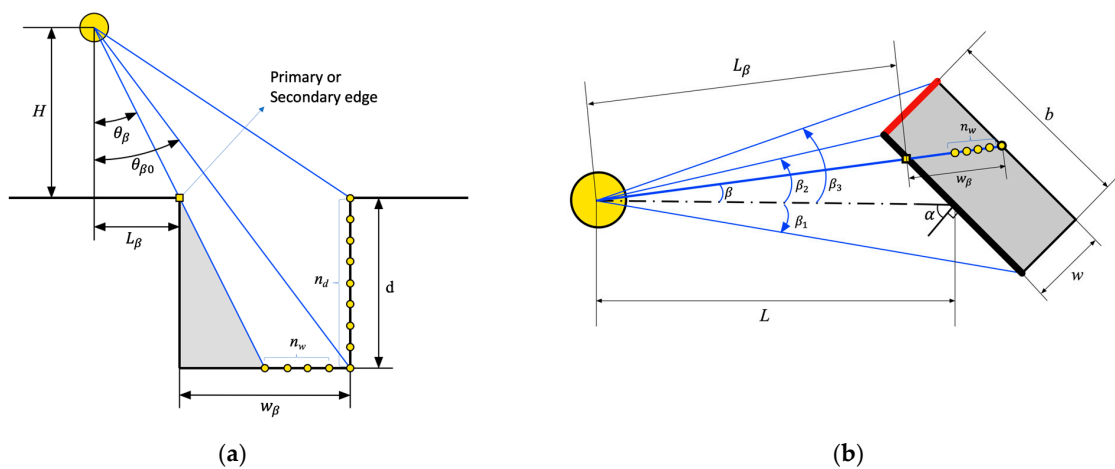


Figure 4. The configuration of the scanner and the opening geometry specimen (a) in the cross-section view and (b) in the plan view.

Table 2. Scan geometric conditions.

Setup Parameter	Value
Set width of the block opening, w (mm)	2, 5, 10, 15, 20
Incidence angle, θ ($^\circ$)	0, 10, 20, 30, 45, 60
Orientation of the block opening, α ($^\circ$)	0, 45, 90

The trigonometric properties shown in Figure 4 can give the following equations to calculate various geometric parameters, with Δ being the scan angle step size of 0.00751° :

$$n_w = \frac{1}{\Delta} \left[\frac{(H \tan \theta_\beta + w_\beta) - \tan \theta_\beta (H+d)}{(H+d) + (H \tan \theta_\beta + w_\beta) \tan \theta_\beta} \right] \quad \text{for } \theta_\beta < \theta_{\beta 0} \quad \text{and} \quad (1)$$

$$n_w = 0 \quad \text{for } \theta_\beta \geq \theta_{\beta 0}$$

$$n_d = \frac{1}{\Delta} \left[\frac{(H \tan \theta_\beta + w_\beta) - H \tan \theta_{\beta 0}}{H + (H \tan \theta_\beta + w_\beta) \tan \theta_{\beta 0}} \right] \quad \text{for } \theta_\beta < \theta_{\beta 0} \quad \text{and} \quad (2)$$

$$n_d = \frac{1}{\Delta} \left[\frac{(H \tan \theta_\beta + w_\beta) - H \tan \theta_\beta}{H + (H \tan \theta_\beta + w_\beta) \tan \theta_\beta} \right] \quad \text{for } \theta_\beta \geq \theta_{\beta 0}$$

$$L_\beta = \frac{L \cot \alpha}{\cos \beta \cot \alpha - \sin \beta} \quad (3)$$

$$\theta_\beta = \arctan(L_\beta / H) \quad \text{and} \quad \theta_{\beta 0} = \arctan\left(\frac{L_\beta + w_\beta}{H + d}\right) \quad (4)$$

$$w_\beta = \frac{w}{\cos(\beta + \alpha)} \quad \text{for the primary edge} \quad (5)$$

$$w_\beta = \frac{w + L(\sin(\beta - \beta_2) / \sin(\beta - \alpha))}{\cos(\beta - \alpha)} \quad \text{for the secondary edge}$$

$$\beta_1 = \arctan\left(\frac{b \cos \alpha}{2L + b \sin \alpha}\right) \quad \text{and} \quad \beta_2 = \arctan\left(\frac{b \cos \alpha}{2L - b \sin \alpha}\right) \quad (6)$$

Using these geometric parameters, one can calculate n_{prime} and n_{second} , the numbers of laser beams that intersect the primary edge line and the secondary edge line, respectively, and n_{total} , the total number of laser beam points reaching the base and vertical face of the opening, as follows:

$$n_{prime} = \sum_{\beta=\beta_1}^{\beta_2} (n_w + n_d), \quad n_{second} = \sum_{\beta=\beta_2}^{\beta_3} (n_w + n_d), \quad \text{and} \quad (7)$$

$$n_{total} = n_{prime} + n_{second}$$

2.4. Detection Level

Figure 5 provides a structured overview of the methodology employed to process the point cloud datasets derived from TLS measurements. Once the scanning phase was concluded, the dataset was transferred to a computer for further evaluation using Leica Cyclone 3dr software (version 2023.0.0.42805) [36]. As depicted in Step 3, following preliminary processing with Leica Cyclone 3dr, the dataset was transitioned to AutoCAD software (version 2022). At this juncture, data points beyond the predefined boundary, highlighted in red, were excluded. Step 4 to 6 involve segmenting the remaining data points of interest into 20 distinct segments. A straight line, representing the top surface of the blocks, is drawn through the 2-dimensional center of the point cloud regions that do not encompass the opening geometry in the cross-sectional view of a chosen segment, as highlighted in Step 7. This aids in identifying edges of the opening geometry where points deviate from the straight line, as depicted in Step 8. In Step 9, the opening width within the selected segment is measured by the distance between two edges facing each other. In instances of excessive noise in the point cloud, hindering edge identification, the corresponding segment dataset is marked as “non-detectable”. Upon processing all 20 segments, the detection level is quantitatively determined by calculating the proportion

of successfully identified segments to the total 20 segments. For example, the detection level reaches 90% when there are two non-detectable segments out of twenty segments.

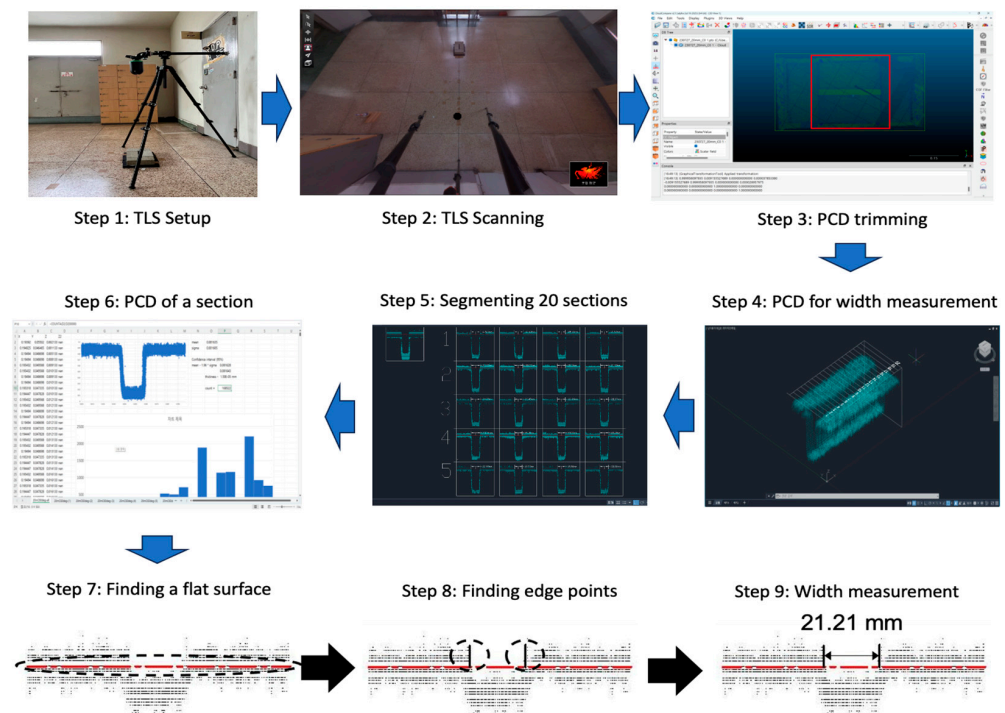


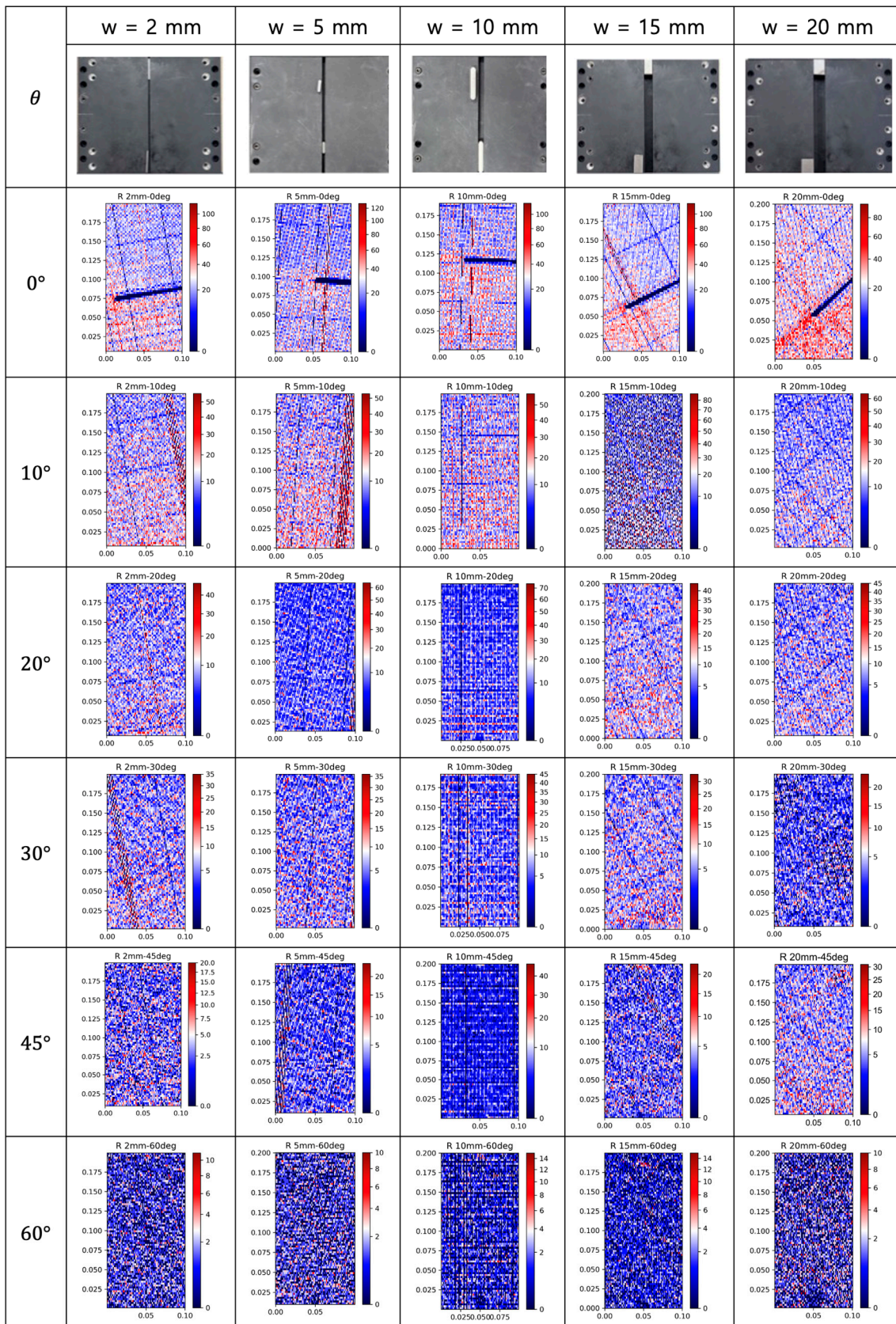
Figure 5. Structured overview of the methodology to process the point cloud datasets.

3. Results

3.1. Point Cloud Density

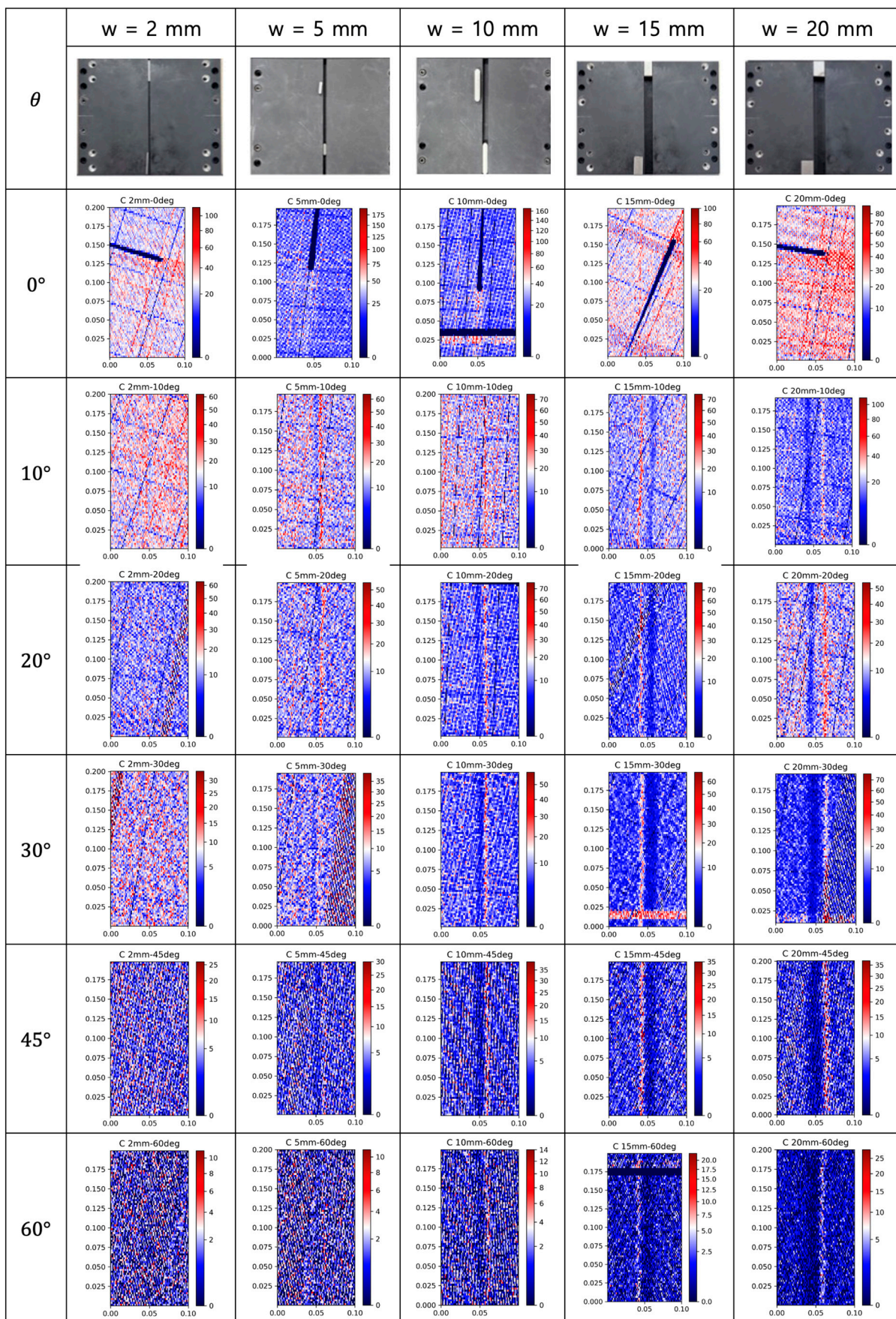
To determine the point cloud density, the dataset from Step 4 in Figure 5 is further processed to remove points outside Zones A and B, shown in Figure 2b. The abscissa and ordinate axes on the horizontal plane are then divided into 100 grid divisions, resulting in 10,000 mesh-like bins when viewed from above. The point cloud density is determined by counting the points within each bin and then dividing by its area.

Figure 6 presents the planar variations in point cloud density using color gradients. Observations from Figure 6a reveal a consistent distribution of data points over the plan view for $\alpha = 90^\circ$, irrespective of variations in the incidence angle (θ) or set width (w). It is evident that the maximal point cloud density occurs at $\theta = 0$. However, this highest density does not necessarily mean the best data quality. In the test conditions with a narrow set width (specifically, $w = 2$ or 5 mm) and small incidence angles ($\theta = 0^\circ$ or 10°), the density distribution for $\alpha = 90^\circ$ is nearly identical to the uniform distribution observed at $\alpha = 0^\circ$ shown in Figure 6b. Conversely, with a wide set width (e.g., $w = 20$ mm) and large incidence angle (e.g., $\theta = 60^\circ$) at $\alpha = 0^\circ$, a distinctive linear pattern emerges, signifying the opening geometry. This pattern deviates from the uniformly distributed point cloud density associated with $\alpha = 90^\circ$. A closer look at Figure 6b for $\alpha = 0^\circ$ reveals noticeable differences in point cloud density near the area encompassing the opening geometry, as indicated by the distinct blue and red linear patterns. This underscores the inherent differences in laser reflection between the vertical face of the opening geometry and the flat horizontal surface of the test specimen. The patterns presented in Figure 6c for $\alpha = 45^\circ$ reflect the trends previously observed in the point cloud density distributions for $\alpha = 0^\circ$. Due to the clear trends noticed for $\alpha = 0^\circ$ and 45° , we assessed the point cloud densities for two distinct zones: the A zone, which covers the opening, and the B zone outside of the A zone. The average point cloud densities for these zones are represented by ρ_A (Zone A) and ρ_B (Zone B). The exact dimensions for Zones A and B have been detailed earlier, in Section 2.2.



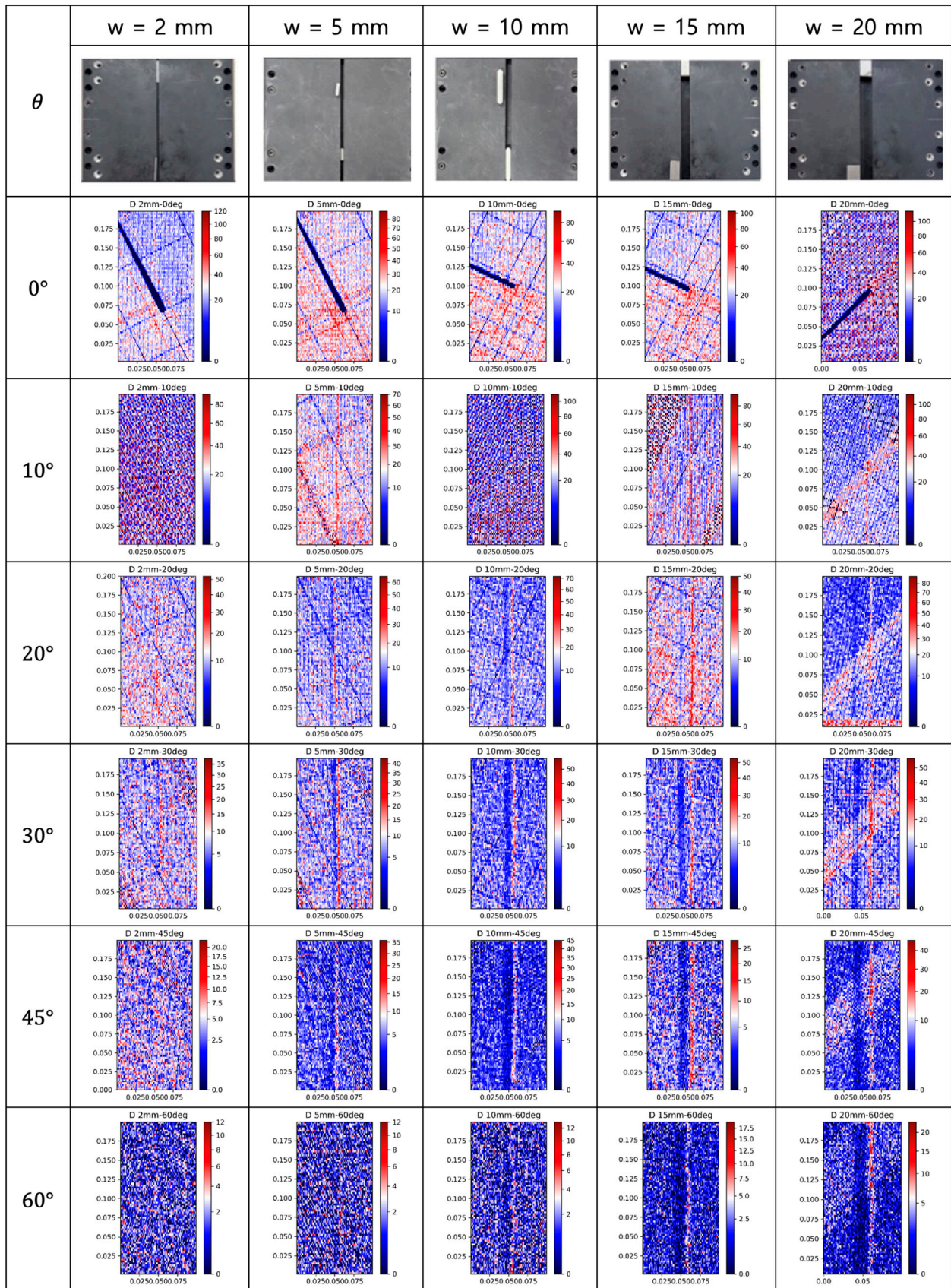
(a) $\alpha = 90^\circ$

Figure 6. Cont.



(b) $\alpha = 0^\circ$

Figure 6. Cont.



(c) $\alpha = 45^\circ$

Figure 6. Planar distribution of point density: (a) $\alpha = 90^\circ$, (b) $\alpha = 0^\circ$, and (c) $\alpha = 45^\circ$. The block opening is positioned at a vertical orientation in the figure.

3.2. Detection Levels

Figure 7 presents the changes in detection level, represented by the numbers in the matrix cell, in correlation with a varying set width, w , and incidence angle, θ . This figure reveals that detection levels remain consistently high at $\alpha = 90^\circ$ for all values of w and θ . However, detection levels are notably influenced by w , with a significant decrease observed for narrower set widths at $\alpha = 0^\circ$ and 45° . Furthermore, when examining the detection level at an incidence angle of $\theta = 60^\circ$ at $\alpha = 0^\circ$ and 45° , capturing the opening geometry becomes unfeasible, even with a large set width of 10 mm. These findings underscore the interplay between geometric factors and their impact on detection levels.

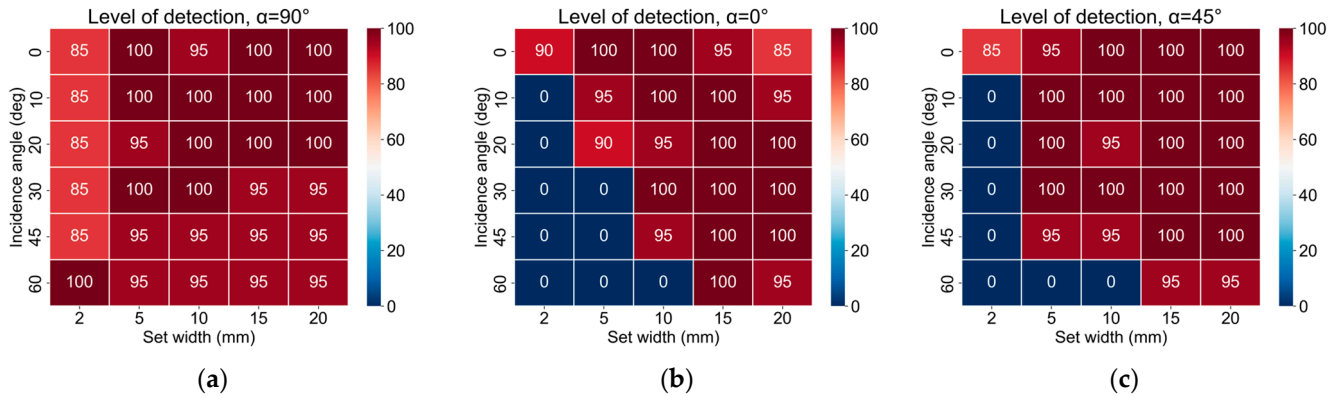


Figure 7. Variation in the detection levels for the different incidence angles and set widths: (a) at $\alpha = 90^\circ$; (b) at $\alpha = 0^\circ$; (c) at $\alpha = 45^\circ$.

In Figure 8, the detection level shows variable degrees of correlation with ρ_A and ρ_B , influenced by the orientation parameter α . At $\alpha = 0^\circ$, a slight positive correlation emerges between the detection level and ρ_A , indicating that a higher point cloud density within Zone A may improve detection capabilities. With α shifting to 45° , the correlation between the detection levels and both ρ_A and ρ_B remain positive, although the scatter of the data points increases, hinting at added complexities in detection introduced by the change in orientation. The correlation becomes more distinct at $\alpha = 90^\circ$, where ρ_A demonstrates a strong positive correlation with the detection level, whereas ρ_B shows a more modest, albeit positive, correlation. These observations are in line with the conclusions drawn by Liu et al. [35], who found that object geometry plays a significant role in the variability in point cloud density, which, in turn, affects the accurate reflection of the geometric features of various targets.

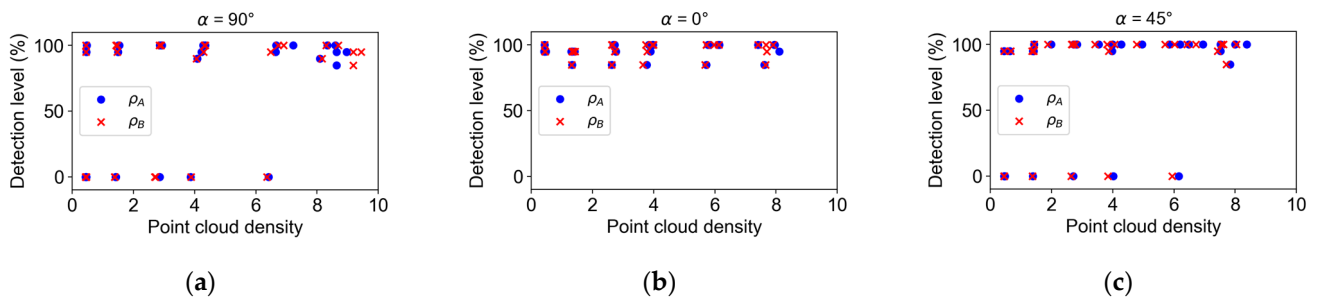


Figure 8. Variation in the detection levels for the different point cloud densities: (a) at $\alpha = 90^\circ$; (b) at $\alpha = 0^\circ$; (c) at $\alpha = 45^\circ$.

In Figure 9, the correlation between the quantity of laser beams and detection accuracy of openings at $\alpha = 90^\circ$, 0° , and 45° is illustrated. At $\alpha = 90^\circ$, an increase in laser beams enhances detection, with the result of n_{second} particularly improving and aligning closely

with that of n_{prime} . However, there appears to be a saturation point beyond which additional beams do not significantly increase the detection level. In the context of $\alpha = 0^\circ$, as shown in Figure 9b, the detection level for n_{prime} remains consistently optimal across varying beam counts. In contrast, at $\alpha = 45^\circ$ in Figure 9c, the detection levels for both n_{prime} and n_{second} evolve with increased beam counts but do so in a coordinated manner. This suggests that the test setup with $\alpha = 45^\circ$ yields results that bridge the outcomes observed at both $\alpha = 0^\circ$ and 90° .

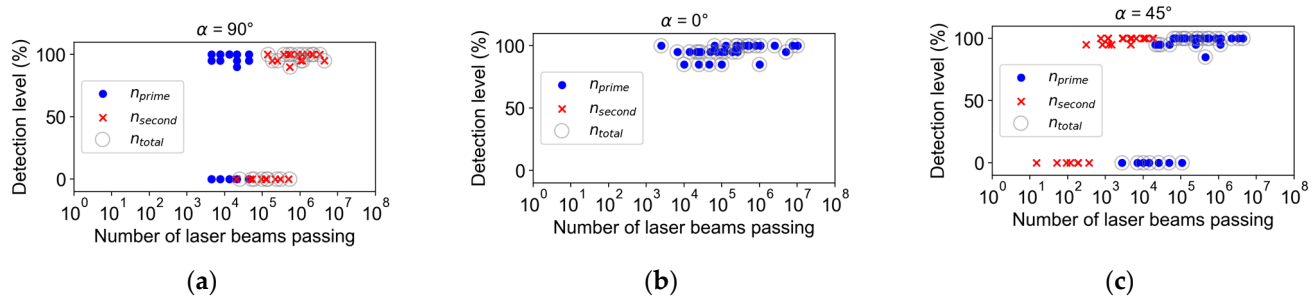


Figure 9. Variation in the detection levels for the different numbers of laser beams passing: (a) at $\alpha = 90^\circ$; (b) at $\alpha = 0^\circ$; (c) at $\alpha = 45^\circ$.

4. Discussion

Although we observed some patterns in the detection levels under various parameters, the hierarchy of their impact is yet to be determined. Soudarissanane et al. [26] identified four principal factors that influence the quality of a scan point procured through TLS: instrumental calibration, atmospheric conditions, object properties, and scanning geometry. Expanding their results, our study focuses on the geometric factors of scanning. For a systematic approach, we divided the following eight parameters into three categories. The first group pertains to the test configurations and scan geometry. It encompasses the set width (w), the orientation of the opening geometry (α), and the incidence angle (θ). The second group includes the total number of laser beam points projected into the opening geometry (n_{total}), the subset that passes the primary edge line (n_{prime}), and those intersecting the secondary edge line (n_{second}). The third group focuses on the point cloud densities in Zone A covering the opening geometry (ρ_A) and the zone outside Zone A (ρ_B).

Figure 10 illustrates the correlation matrix, detailing the Pearson's correlation values between the detection level and eight parameters. The highest positive correlation to the detection level can be found at the set width, w , while the highest negative correlation can be found at the orientation of the opening geometry, α . Although Figure 10 allows for the ranking of the influencing parameters based on correlation values, it is essential to note that Pearson correlation primarily measures linear relationships. However, as seen in Figures 8 and 9, our data do not always demonstrate a linear relationship between parameters and detection level. Hence, examining other metrics becomes essential to capture the underlying patterns more accurately. Herein, we have used nine ranking metrics to further investigate the influence of various parameters on detection levels. Their characteristics and specialties are outlined in Table 3.

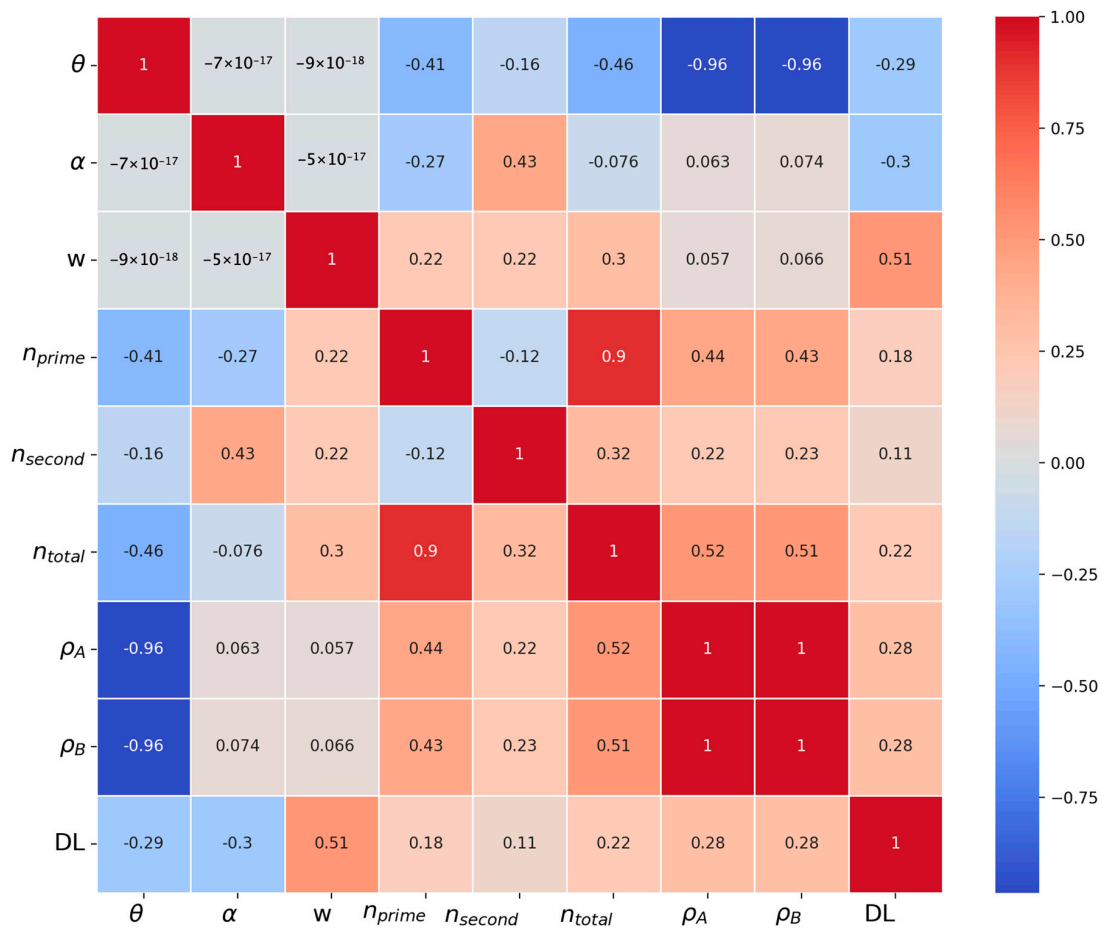


Figure 10. Correlation matrix detailing the Pearson’s correlation values between the detection level and eight parameters. “DL” in the chart denotes the detection level.

Table 3. Comparison of ranking metrics: characteristics and specialties.

Ranking Metrics	General Characteristics	Specialty
Pearson correlation coefficient	Measures linear relationship between two variables	Simple, widely used for continuous variables
Partial correlation	Measures linear relationship between two variables and controls for the effects of another set of variables	Accounts for potential confounding variables
Mutual information	Measures dependence between variables, can capture non-linear relationships	Detects any kind of relationship (non-linear included)
Multivariate linear regression	Explores relationship between two or more variables	Can rank the importance of predictors for a given response
Principal component analysis	Transforms original variables into orthogonal set	Extracts most informative features; dimension reduction
Random forest analysis	Ensemble tree-based learning method	Offers feature importance ranking out of the box
Lasso regression analysis	Linear regression with L1 regularization	Feature selection by shrinking some coefficients to 0
Elastic Net analysis	Combines L1 and L2 regularization of LASSO and Ridge	Addresses multicollinearity; feature selection
XGBoost analysis	Gradient-boosted tree-based method	High performance; provides feature importance scores

Figure 11 presents the ranking of influencing parameters on detection levels using nine different metrics. The Pearson correlation measures the linear relationship between

variables, with the bar length and direction representing the correlation strength and type, respectively. The partial correlation refines this by accounting for other variables, highlighting a direct relationship, with standardized coefficients offering insights. The mutual information (MI) scores emphasize variable interdependency, where a higher score indicates a stronger relationship. Linear regression examines the relationship between a dependent variable and its predictors, with bar lengths denoting coefficient significance. Principal component analysis (PCA) addresses dimensionality reduction, illustrating each factor’s contribution to the primary component. Random forest evaluates factors’ importance based on their prevalence in decision trees. LASSO regression incorporates a penalty for non-zero coefficients, leading to potential feature selection, with bar lengths denoting coefficient significance. Elastic net regression combines LASSO and ridge regression attributes, with the bars indicating coefficient magnitude. Finally, XGBoost assigns importance scores to each factor.

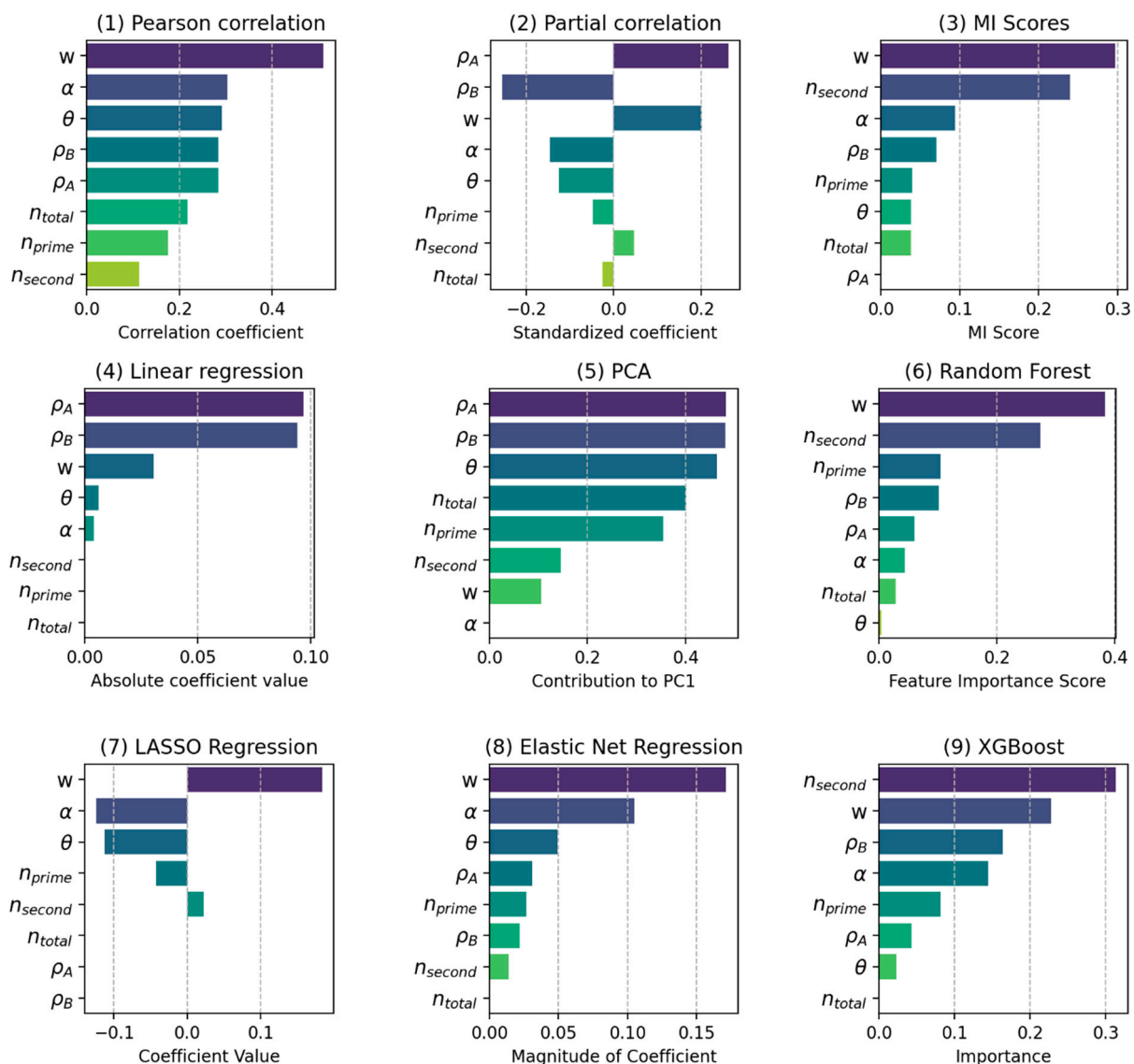


Figure 11. Ranked lists of nine different metrics.

Figure 12 presents the final ranking of influencing parameters on the detection level of opening geometry using point cloud data. This ranking is determined based on the Borda count of the parameters, as shown in Figure 11. The Borda count is a ranking-based voting method where voters order choices, and points are assigned based on these

rankings. This approach is useful for aggregating the preferences of multiple evaluators, i.e., nine different metrics herein, in a way that accounts for the relative rankings of all options [37,38]. The opening width, w , emerges as the paramount parameter, implying that wider openings increase detection levels. Interestingly, ρ_B exhibits an advantage over ρ_A slightly, emphasizing the primacy of point cloud density on flat surfaces over surfaces with local geometry. Hence, a general enhancement in point density assumes greater significance than localized density disparities. The high ranking of both ρ_A and ρ_B indicates that the relationship between point cloud density and geometric parameters might be intricate. Among the geometric parameters considered, w clearly outweighs both α and θ in influence. Notably, α takes precedence over θ , suggesting that the orientation of the local geometry is more influential than its angle of incidence. Theoretically computed numbers of the laser beam point, specifically n_{prime} , n_{second} , and n_{total} , are ranked lower. This indicates that merely amplifying the number of beam points inside the opening is not a guaranteed strategy for improved detection. Among these, n_{second} stands out, suggesting that for optimal detection, laser beams traversing the secondary edge are more consequential than those on the primary edge.

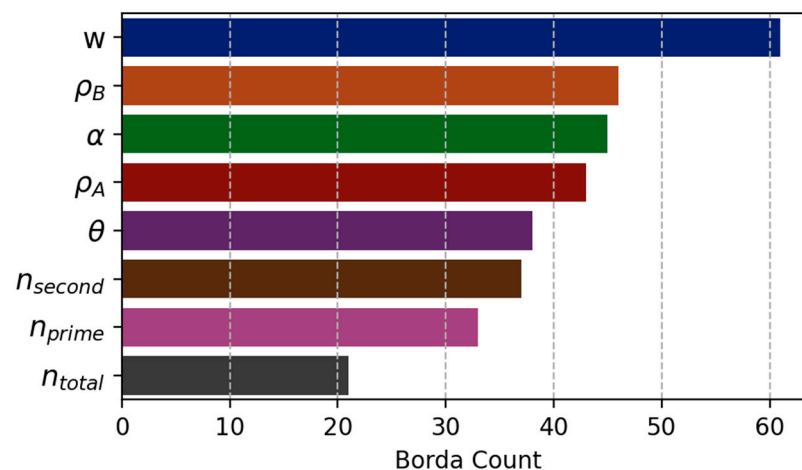


Figure 12. Borda count of the influencing parameters.

In summarizing the findings of our study, it is imperative to acknowledge certain limitations that could influence the generalizability of our results. Primarily, the exclusive use of the BLK360 scanner may limit the applicability of our findings across various static TLS devices. It is worth noting that there can be significant differences in the quality of data scanned by various 3D laser scanners, as reported by Boehler et al. [7]. As detailed by Petrie and Toth [39] in their comprehensive comparison of TLS systems, different scanners vary in technical specifications, which can potentially affect data accuracy and precision. According to Soudarissanane et al. [23], two major influencing factors related to scanning geometry—the incidence angle and range—are crucial, as they directly influence the signal-to-noise ratio and the precision of measurements of planar surfaces. Soudarissanane [25] found that the range effect model is dependent on the laser scanner model used. In our study, the ranges in our test setups were less than 3 m, and their effect on signal deterioration was insignificant. We observed the same pattern of signal deterioration with increasing incidence angle, as depicted in Figure 7. Interestingly, we found that the orientation of the local opening geometry, which also defines the scanning geometry, is as crucial as the incidence angle.

Our research utilized a specific geometry of block opening, raising uncertainties about the replication of our conclusions in scenarios involving different geometrical forms, like holes or irregular cracks. Additionally, the absence of a diverse range of case studies, particularly in more open environments, is a practical limitation. Environmental factors, such as light intensity, humidity, and other conditions, distinct from geometric factors, play

a significant role in TLS accuracy in open settings. However, these factors are not accounted for in the current study, and thus, their impacts warrant separate investigation.

5. Conclusions

This study investigated different parameters influencing the detection level of opening geometries using point cloud data acquired using the BLK360 laser scanner. Our findings underscore the significance of several key parameters:

- (1) **Opening width:** The width of the opening proved to be a crucial parameter. Larger openings notably enhance detection levels, with a rectangular shape in a 2D cross-sectional view becoming more distinct as the space between blocks expands. Under our test configuration, we guarantee the detection of openings wider than 10 mm.
- (2) **Point cloud density:** The broad increase in point density is more significant than specific localized density variations. This indicates a complex relationship between the point cloud density and geometric parameters, where object geometry is a key factor in point cloud density variations, thereby influencing the precise depiction of geometric characteristics in different targets.
- (3) **Geometric parameters:** Among the geometric parameters considered, the orientation of the local geometry (α) holds more weight than its angle of incidence (θ). Under our testing setup, we ensure the detection of an opening geometry with $\alpha = 90^\circ$.
- (4) **Laser beam points:** Theoretically computed numbers for the laser beam point are given lower priority. This suggests that simply increasing the beam points inside an opening does not necessarily enhance detection levels. It is worth noting that n_{second} is prominent, suggesting that laser beams crossing the secondary edge have greater impact than those on the primary edge.

There are limitations associated with the use of a single BLK360 scanner, which may affect the generalizability of findings across various TLS devices due to differences in data quality and technical specifications, as reported in previous research. Two factors related to scanning geometry, incidence angle and range, significantly influence data precision. The study's tests showed negligible range effects under 3 m but confirmed signal deterioration with increasing incidence angles, a pattern consistent with prior findings. Additionally, the orientation of the local opening geometry, which also defines the scanning geometry, was identified as a critical factor, highlighting the nuanced impact of scanner-specific characteristics on data accuracy and reliability.

Author Contributions: Conceptualization, T.K. and Y.-H.J.; methodology, T.K.; software, S.K.; validation, J.J. and H.M.; formal analysis, S.K.; investigation, S.K. and Y.-H.J.; resources, Y.-H.J.; data curation, J.J. and H.M.; writing—original draft preparation, Y.-H.J.; writing—review and editing, J.J. and T.K.; visualization, S.K. and H.M.; supervision, T.K.; project administration, Y.-H.J.; funding acquisition, Y.-H.J. All authors have read and agreed to the published version of the manuscript.

Funding: This work was supported by a National Research Foundation of Korea (NRF) grant funded by the Korean government (MSIT) (2019R1A2C1089155).

Data Availability Statement: Data available on request from the authors. The data that support the findings of this study are available from the corresponding author, Y.-H.J., upon request.

Acknowledgments: We thank Hyunseok Hong for his pivotal role in conducting the terrestrial laser scanning experiments, a core part of his Master's thesis, which significantly contributed to this research.

Conflicts of Interest: The authors declare no conflicts of interest.

References

1. Wu, C.; Yuan, Y.; Tang, Y.; Tian, B. Application of Terrestrial Laser Scanning (TLS) in the Architecture, Engineering and Construction (AEC) industry. *Sensors* **2022**, *22*, 265. [CrossRef]
2. Leica Geosystems. Leica BLK360 Imaging Laser Scanner. 2023. Available online: <https://leica-geosystems.com/en-us/products/laser-scanners/scanners/blk360> (accessed on 18 February 2024).

3. González-Jorge, H.; Riveiro, B.; Armesto, J.; Arias, P. Procedure to evaluate the accuracy of laser-scanning systems using a linear precision electro-mechanical actuator. *IET Sci. Meas. Technol.* **2012**, *6*, 6–12. [[CrossRef](#)]
4. Nguyen, A.C.; Weinand, Y. Displacement study of a large-scale freeform timber plate structure using a total station and a terrestrial laser scanner. *Sensors* **2020**, *20*, 413. [[CrossRef](#)]
5. Gordon, S.; Lichti, D.; Stewart, M.; Franke, J. Structural deformation measurement using terrestrial laser scanners. In Proceedings of the 11th International FIG Symposium on Deformation Measurements, Santorini, Greece, 25–28 May 2003.
6. Lichti, D.; Gordon, S.; Stewart, M.; Franke, J.; Tsakiri, M. Comparison of digital photogrammetry and laser scanning. In Proceedings of the International Society for Photogrammetry and Remote Sensing, Graz, Austria, 9–13 September 2002.
7. Boehler, W.; Bordas, V.; Marbs, A. Investigating laser scanner accuracy. *Int. Arch. Photogramm. Remote Sens. Spat. Inf. Sci.* **2003**, *34*, 696–701.
8. Olsen, M.; Kuester, F.; Chang, B.; Hutchinson, T. Terrestrial laser scanning-based structural damage assessment. *J. Comput. Civ. Eng.* **2010**, *24*, 264–272. [[CrossRef](#)]
9. Valença, J.; Puente, I.; Júlio, E.; González-Jorge, H.; Arias-Sánchez, P. Assessment of cracks on concrete bridges using image processing supported by laser scanning survey. *Constr. Build. Mater.* **2017**, *146*, 668–678. [[CrossRef](#)]
10. Cho, S.; Park, S.; Cha, G.; Oh, T. Development of image processing for crack detection on concrete structures through terrestrial laser scanning associated with the octree structure. *Appl. Sci.* **2018**, *8*, 2373. [[CrossRef](#)]
11. Zhou, S.; Song, W. Deep learning-based roadway crack classification using laserscanned range images: A comparative study on hyperparameter selection. *Autom. Constr.* **2020**, *114*, 103171. [[CrossRef](#)]
12. Suchocki, C. Comparison of time-of-flight and phase-shift TLS intensity data for the diagnostics measurements of buildings. *Materials* **2020**, *13*, 353. [[CrossRef](#)]
13. Yang, H.; Xu, X. Intelligent crack extraction based on terrestrial laser scanning measurement. *Meas. Control* **2020**, *53*, 416–426. [[CrossRef](#)]
14. Stałowska, P.; Suchocki, C.; Rutkowska, M. Crack detection in building walls based on geometric and radiometric point cloud information. *Autom. Constr.* **2022**, *134*, 104065. [[CrossRef](#)]
15. Yang, X.; Hui, B.; Lu, B.; Yuan, B.; Li, Y. Effect of 3D laser point spacing on cement concrete crack width measurement. *Meas. Sci. Technol.* **2023**, *34*, 085018. [[CrossRef](#)]
16. Cabaleiro, M.; Lindenbergh, R.; Gard, W.F.; Arias, P.; Van De Kuilen, J.W.G. Algorithm for automatic detection and analysis of cracks in timber beams from LiDAR data. *Constr. Build. Mater.* **2017**, *130*, 41–53. [[CrossRef](#)]
17. Laefer, D.F.; Truong-Hong, L.; Carr, H.; Singh, M. Crack detection limits in unit based masonry with terrestrial laser scanning. *NDT E Int.* **2014**, *62*, 66–76. [[CrossRef](#)]
18. Nyathi, M.A.; Bai, J.; Wilson, I.D. Concrete crack width measurement using a laser beam and image processing algorithms. *Appl. Sci.* **2023**, *13*, 4981. [[CrossRef](#)]
19. Laefer, D.F.; Fitzgerald, M.; Maloney, E.M.; Coyne, D.; Lennon, D.; Morrish, S.W. Lateral image degradation in terrestrial laser scanning. *Struct. Eng. Int.* **2009**, *19*, 184–189. [[CrossRef](#)]
20. Teng, J.; Shi, Y.; Wang, H.; Wu, J. Review on the research and applications of TLS in ground surface and constructions deformation monitoring. *Sensors* **2023**, *22*, 9179. [[CrossRef](#)] [[PubMed](#)]
21. Stenz, U.; Hartmann, J.; Paffenholz, J.A.; Neumann, I. A framework based on reference data with superordinate accuracy for the quality analysis of terrestrial laser scanning-based multi-sensor-systems. *Sensors* **2017**, *17*, 1886. [[CrossRef](#)]
22. Pawłowicz, J.A. Effect of geometrical features various objects on the data quality obtained with measured by TLS. *IOP Conf. Ser. Mater. Sci. Eng.* **2017**, *227*, 012093. [[CrossRef](#)]
23. Soudarissanane, S.S.; Lindenbergh, R.; Menenti, M.; Teunissen, P. Scanning geometry: Influencing factor on the quality of terrestrial laser scanning points. *ISPRS J. Photogramm. Remote Sens.* **2011**, *66*, 389–399. [[CrossRef](#)]
24. Soudarissanane, S.S. The Geometry of Terrestrial Laser Scanning. Ph.D. Thesis, Delft University of Technology, Delft, The Netherlands, 5 January 2016.
25. Soudarissanane, S.; Lindenbergh, R.; Gorte, B. Reducing the error in terrestrial laser scanning by optimizing the measurement setup. *Int. Arch. Photogramm. Remote Sens. Spat. Inf. Sci.* **2008**, *XXXVII*, 615–620.
26. Wei, F.; Xianfeng, H.; Fan, Z.; Deren, L. Intensity correction of terrestrial laser scanning data by estimating laser transmission function. *IEEE Trans. Geosci. Remote Sens.* **2014**, *53*, 942–951. [[CrossRef](#)]
27. Krooks, A.; Kaasalainen, S.; Hakala, T.; Nevalainen, O. Correction of intensity incidence angle effect in terrestrial laser scanning. *ISPRS Ann. Photogramm. Remote Sens. Spat. Inf. Sci.* **2013**, *2*, 145–150. [[CrossRef](#)]
28. Kaasalainen, S.; Jaakkola, A.; Kaasalainen, M.; Krooks, A.; Kukko, A. Analysis of incidence angle and distance effects on terrestrial laser scanner intensity: Search for correction methods. *Remote Sens.* **2011**, *3*, 2207–2221. [[CrossRef](#)]
29. Roca-Pardiñas, J.; Argüelles-Fraga, R.; De Asís López, F.; Ordóñez, C. Analysis of the influence of range and angle of incidence of terrestrial laser scanning measurements on tunnel inspection. *Tunneling Undergr. Space Technol.* **2014**, *43*, 133–139. [[CrossRef](#)]
30. Lichti, D.D.; Jamtsho, S.; El-Halawany, S.I.; Lahamy, H.; Chow, J.; Chan, T.O.; El-Badry, M. Structural deflection measurement with a range camera. *J. Surv. Eng.* **2012**, *138*, 66–76. [[CrossRef](#)]
31. Milenkovic, M.; Pfeifer, N.; Glira, P. Applying terrestrial laser scanning for soil surface roughness assessment. *Remote. Sens.* **2015**, *7*, 2007–2045. [[CrossRef](#)]

32. Tesfamariam, E.K. Comparing Discontinuity Surface Roughness Derived from 3D Terrestrial Laser Scan Data with Traditional Field-Based Methods. Master's Thesis, Delft University of Technology, Delft, The Netherlands, 2007.
33. Abegg, M.; Boesch, R.; Schaepman, M.E.; Morsdorf, F. Impact of beam diameter and scanning approach on point cloud quality of terrestrial laser scanning in forests. *IEEE Trans. Geosci. Remote Sens.* **2020**, *59*, 8153–8167. [[CrossRef](#)]
34. Gerbino, S.; Del Giudice, D.M.; Staiano, G.; Lanzotti, A.; Martorelli, M. On the influence of scanning factors on the laser scanner-based 3D inspection process. *Int. J. Adv. Manuf. Technol.* **2016**, *84*, 1787–1799. [[CrossRef](#)]
35. Liu, S.; Tan, K.; Tao, P.; Yang, J.; Zhang, W.; Wang, Y. Rigorous density correction model for single-scan TLS point clouds. *IEEE Trans. Geosci. Remote Sens.* **2023**, *61*, 1–18. [[CrossRef](#)]
36. Leica Geosystems. *Cyclone 3dr*; Version 2023.0.0.42805; Computer software; Leica Geosystems: St. Gallen, Switzerland, 2023. Available online: <https://leica-geosystems.com/products/laser-scanners/software/leica-cyclone/leica-cyclone-3dr> (accessed on 18 February 2024).
37. Saari, D.G. Selecting a voting method: The case for the Borda count. *Const. Political Econ.* **2023**, *34*, 357–366. [[CrossRef](#)]
38. Borda Count. Available online: https://en.wikipedia.org/wiki/Borda_count (accessed on 14 January 2024).
39. Petrie, G.; Toth, C.K. Terrestrial Laser Scanners. In *Topographic Laser Ranging and Scanning: Principles and Processing*, 2nd ed.; Shan, J., Toth, C.K., Eds.; Taylor & Francis: Oxfordshire, UK; CRC Press: Boca Raton, FL, USA; pp. 29–88.

Disclaimer/Publisher's Note: The statements, opinions and data contained in all publications are solely those of the individual author(s) and contributor(s) and not of MDPI and/or the editor(s). MDPI and/or the editor(s) disclaim responsibility for any injury to people or property resulting from any ideas, methods, instructions or products referred to in the content.